



## Adaptive scheduling of acceleration and gyroscope for motion artifact cancellation in photoplethysmography

Hooseok Lee<sup>a</sup>, Heewon Chung<sup>a</sup>, Hoon Ko<sup>a</sup>, Antonino Parisi<sup>b</sup>, Alessandro Busacca<sup>b</sup>, Luca Faes<sup>b</sup>, Riccardo Pernice<sup>b,\*\*</sup>, Jinseok Lee<sup>a,\*</sup>

<sup>a</sup> Department of Biomedical Engineering, Kyung Hee University, Yongin, 17104 Korea

<sup>b</sup> Department of Engineering, University of Palermo, 90128 Palermo Italy

### ARTICLE INFO

#### Article history:

Received 5 July 2022

Revised 30 August 2022

Accepted 11 September 2022

#### Keywords:

Reflectance-type photoplethysmography (PPG)

Instantaneous heart rate (HR)

Adaptive motion artifact reference selection

Acceleration signal

Gyroscope signal

### ABSTRACT

**Background and objective:** Recently, various algorithms have been introduced using wrist-worn photoplethysmography (PPG) to provide high accuracy of instantaneous heart rate (HR) estimation, including during high-intensity exercise. Most studies focus on using acceleration and/or gyroscope signals for the motion artifact (MA) reference, which attenuates or cancels out noise from the MA-corrupted PPG signals. We aim to open and pave the path to find an appropriate MA reference selection for MA cancelation in PPG.

**Methods:** We investigated how the acceleration and gyroscope reference signals correlate with the MAs of the distorted PPG signals and derived both mathematically and experimentally an adaptive MA reference selection approach. We applied our algorithm to five state-of-the-art (SOTA) methods for the performance evaluation. In addition, we compared the four MA reference selection approaches, i.e. with acceleration signal only, with gyroscope signal only, with both signals, and using our proposed adaptive selection.

**Results:** When applied to 47 PPG recordings acquired during intensive physical exercise from two different datasets, our proposed adaptive MA reference selection method provided higher accuracy than the other MA selection approaches for all five SOTA methods.

**Conclusion:** Our proposed adaptive MA reference selection approach can be used in other MA cancellation methods and reduces the HR estimation error.

**Significance:** We believe that this study helps researchers to address acceleration and gyroscope signals as accurate MA references, which eventually improves the overall performance for estimating HRs through the various algorithms developed by research groups.

© 2022 The Authors. Published by Elsevier B.V.

This is an open access article under the CC BY license (<http://creativecommons.org/licenses/by/4.0/>)

## 1. Introduction

Wrist-worn photoplethysmography (PPG) sensors have attracted considerable attention because they can conveniently monitor instantaneous heart rate (HR) in real time. A wrist-worn PPG sensor is usually a reflective type, which transmits light on a wrist and identifies the arterial blood volume change by the amount of reflected light during the systolic and diastolic phases of the cardiac cycle. Compared to the transmissive type, the sensor placement is not restricted to any particular measurement site [1,2]. This convenient measurement method can be used in various medical applications such as home-based cardiac rehabilitation [3–5], automatic

cardiac disease detection [6–9], HR dynamics analysis [10–13], and autonomic systems to respond to stressors [14,15]. The wrist-worn PPG is sensitive to motion artifacts (MAs), which usually originate from the movement applied on the wrist during daily activities. Thus, it is challenging to consistently estimate accurate instantaneous HRs. To overcome the MA issue, hardware or algorithmic approach was considered. In [16], ensemble empirical mode decomposition with principal component analysis was used for effectively denoising PPG signals. In [17], nine-multichannel device for PPG signal acquisition was considered. Then, the multichannel signals were denoised by using truncated singular value decomposition. However, both studies are not available to the PPG signals severely corrupted by MAs because MA reference such as acceleration signals were not considered. Indeed, the study [16] validated the algorithm using only MIMIC data, which contains intensive care unit patients with little movement. The algorithm [17] provided rela-

\*\* Co-corresponding author.

\* Corresponding author.

E-mail addresses: [riccardo.pernice@unipa.it](mailto:riccardo.pernice@unipa.it) (R. Pernice), [gonasago@khu.ac.kr](mailto:gonasago@khu.ac.kr) (J. Lee).

tively high absolute error around 4 beats per minute (bpm) because of the lack of MA references.

In recent years, numerous MA cancelation algorithms have been introduced using acceleration signals to provide high accuracy of HR estimation [18–29], including during high-intensity exercise. In most studies, the MAs corrupting PPG signal were attenuated or cancelled out by using acceleration signals measured simultaneously with PPG signals as the MA reference. In [18], the algorithm imposed a common sparsity constraint on spectral coefficients based on the power spectrum of PPG and acceleration signals. In [19], the algorithm removed noise via ensemble empirical mode decomposition, and the power spectrum peak from acceleration signals were excluded for HR estimation. In [20], the algorithm used a frequency based-Wiener filter to attenuate the MAs using acceleration signals. In [21], HR was estimated with signal decomposition approach, where acceleration-based high-resolution spectrum estimation was employed to remove MAs, followed by spectral peak tracking and verification. Those studies improved the HR estimation accuracy providing approximately 2-3 bpm of absolute errors. In [22–24], Bayesian-based prediction algorithms were further considered for tracking HR. For the HR state update, the power spectrum of acceleration signals was used for attenuating MA frequency power. In [25], the concept of a finite state machine was used after MA removal from acceleration signals. The method automatically provides only accurate HR estimation results in real-time by ignoring the estimation results from severely-corrupted PPG signals. In [26], convolutional neural networks were introduced using the inputs of time-frequency spectrum of the PPG and acceleration signals. In [28], HR was estimated by peak detection in time-domain. The acceleration signals confirmed the reliability of PPG signals. In [29], power spectra of PPG and acceleration signals were applied to a modified Wiener filter by emphasizing the power of the frequency corresponding to the previous window HR estimation results. However, in our previous study, we addressed the limitations of accelerometers, which measure not only the acceleration of motion, but also the gravitational acceleration [30]. Gyroscope signals can replace the acceleration signals and thus be used as an alternative MA reference. However, a gyroscope sensor measures angular velocity in the direction of rotation, which cannot fully represent MAs corrupting PPG signals. Recently, both acceleration and gyroscope signals have been used for the MA references [31–33], but most studies focus on simply combining acceleration and gyroscope signals for the MA reference.

In this study, we aim to open and pave the path for finding an appropriate MA reference selection. For more accurate MA cancelation, we present an in-depth analysis of how the acceleration and gyroscope signals correlate with the MAs of the distorted PPG signals. To the best of our knowledge, the analysis of the acceleration and gyroscope signal characteristics for MA reference identification has still not been addressed. Furthermore, we propose an adaptive MA reference selection approach for the acceleration and gyroscope signals. Such an adaptive scheduling is to use more appropriate MA reference to increase the HR estimation accuracy. We believe that this study helps researchers to address acceleration and gyroscope signals as accurate MA references, which eventually improves the overall performance of HR estimation through the various algorithms developed by each research group.

## 2. Problem description and motivation

In order to explain the necessity of this study, we conducted a simple experiment in which one subject wore a reflective PPG sensor on the wrist and ran on a treadmill. Using our wrist-worn PPG sensor described in [30], we also measured three-axis accelerometer signals and three-axis gyroscope signals using the inertial measurement unit (IMU) sensor. A chest electrocardiography (ECG) sig-

nal was simultaneously recorded and used to extract the gold standard HRs. All signals were sampled at 125 Hz. Throughout this study, we used 8s window with 2-s shifts (thus 6-s of overlap) for all signals, which estimates HR value every 2-s. We used the same window length (8-s) and shift (2-s) to assess the performance of our algorithm, similarly to what done by the authors of previous algorithms [16–29]. For the  $i$ th window, we used PPG signal  $S(i)$ , the three-axis accelerometer signals  $A_x(i)$ ,  $A_y(i)$ , and  $A_z(i)$ , and the gyroscope-axis gyroscope signals,  $G_x(i)$ ,  $G_y(i)$ , and  $G_z(i)$ . We first filtered  $S(i)$  using a fourth-order Butterworth band pass filter (BPF) with cutoff frequencies of 0.4 Hz and 4 Hz, which range covers the HR range between 0.6 and 3.3 Hz of subjects of all ages when both resting and engaging in intensive physical activity [34,35]. Then, we normalized  $S(i)$  to zero mean with unit variance:

$$S_n(i) = \frac{S(i) - \mu(S(i))}{\sigma(S(i))}, \quad (1)$$

where  $\mu(\cdot)$  and  $\sigma(\cdot)$  are the mean and standard deviation, and  $S_n(i)$  is the normalized PPG signal. In the same way, we also normalized the three-axis accelerometer signals and the gyroscope signals, and averaged them as

$$\begin{aligned} A_n(i) &= \frac{1}{3} \times \left( \frac{A_x(i) - \mu(A_x(i))}{\sigma(A_x(i))} + \frac{A_y(i) - \mu(A_y(i))}{\sigma(A_y(i))} + \frac{A_z(i) - \mu(A_z(i))}{\sigma(A_z(i))} \right) \\ G_n(i) &= \frac{1}{3} \times \left( \frac{G_x(i) - \mu(G_x(i))}{\sigma(G_x(i))} + \frac{G_y(i) - \mu(G_y(i))}{\sigma(G_y(i))} + \frac{G_z(i) - \mu(G_z(i))}{\sigma(G_z(i))} \right), \end{aligned} \quad (2)$$

where  $A_n(i)$  and  $G_n(i)$  are the normalized and averaged acceleration and gyroscope signals, respectively. The signals  $S_n(i)$ ,  $A_n(i)$ ,  $G_n(i)$  were then down-sampled to 25 Hz. Subsequently, we computed power spectra  $P_S(i)$ ,  $P_A(i)$  and  $P_G(i)$  from  $S_n(i)$ ,  $A_n(i)$ ,  $G_n(i)$ , respectively. Fig. 1(a) and (d) show the two different examples (the case 1 in Fig. 1(a), and the case 2 in Fig. 1(d)) representing the power spectra  $P_S(i)$ ,  $P_A(i)$  and  $P_G(i)$ : PPG (blue), acceleration (red), and gyroscope (green) signals when a subject ran on a treadmill with a true HR of approximately 2 Hz. In Fig. 1(a),  $P_S(i)$  exhibits a dominant frequency power of approximately 2.8 Hz, indicating that the dominant frequency of the PPG signal does not overlap with the true HR (2 Hz). Similarly, in Fig. 1(d),  $P_S(i)$  exhibits a dominant frequency power of approximately 1.2 Hz, which does not overlap with the true HR (2 Hz).

For the MA cancelation, we consider Wiener filter, which is to estimate a desired signal by linear time-invariant filtering of an observed noisy process. For the measured PPG spectrum  $P_S(i)$  corrupted by uncorrelated additive random noise, the frequency-domain Wiener filter is given by

$$P_C(i) \approx P_S(i) - P_A(i) = \left( \frac{P_S(i) - P_A(i)}{P_S(i)} \right) P_S(i) \approx \left( \frac{P_C(i)}{P_C(i) + P_A(i)} \right) P_S(i) \quad (3)$$

where  $P_C(i)$  and  $P_A(i)$  are the spectra of the MA-free PPG signal and acceleration signal as the MA reference, respectively. Similarly,  $P_C(i) \approx P_S(i) - P_G(i)$ , if we use the gyroscope signal as the MA reference. Assuming that the power spectra  $P_C(i-1)$  and  $P_C(i)$  in consecutive windows nearly overlap,  $P_C(i)$  can be substituted with  $P_C(i-1)$ . Then,  $P_C(i)$  can be recursively estimated as [20]

$$P_C(i) = \left( \frac{P_C(i-1)}{P_C(i-1) + P_A(i)} \right) P_S(i). \quad (4)$$

For the gyroscope signal based MA cancelation,

$$P_C(i) = \left( \frac{P_C(i-1)}{P_C(i-1) + P_G(i)} \right) P_S(i). \quad (5)$$

Fig. 1(b) and (c) show the estimated MA-free PPG power spectra  $P_C(i)$  using the acceleration and gyroscope signals, respectively for the case 1 (Fig. 1(a)). Similarly, Fig. 1(e) and (f) show the estimated clear PPG power spectra  $P_C(i)$  using the acceleration and gyroscope signals, respectively for Case 2 (Fig. 1(d)). In the case 1, the

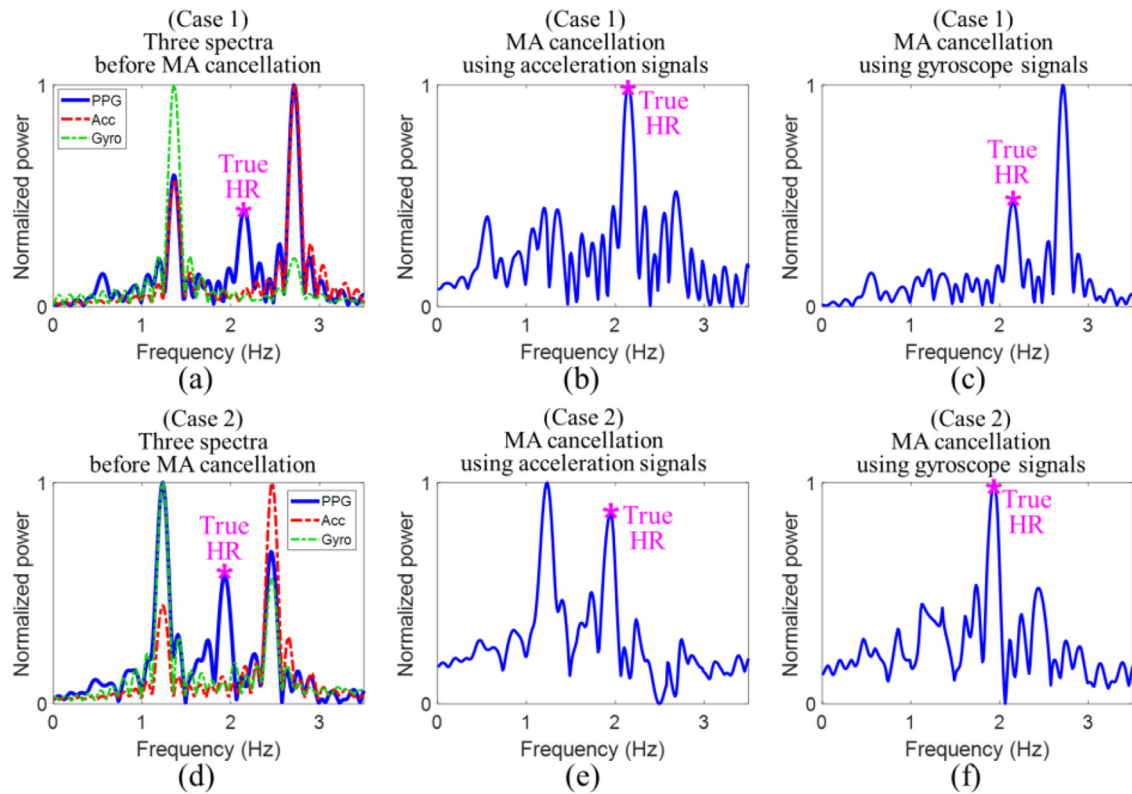


**Fig. 1.** Acceleration and gyroscope signals may provide different MA cancellation results (a) – (c): example 1 in which only the acceleration signal correctly cancels out the true MAs in the PPG signal; (d) – (f): example in which the gyroscope signal only correctly cancels out the true MAs in the PPG signal. (a) Resultant three spectra in case of example 1 from PPG (blue), acceleration (red), and gyroscope (green) signals (true HR extracted from ECG is approximately 2 Hz); PPG power spectrum after MA cancellation using (b) acceleration signal and (c) gyroscope signal. (d) Resultant three spectra in case of example 2 from PPG (blue), acceleration (red), and gyroscope (green) signals (true HR extracted from ECG is approximately 2 Hz); PPG power spectrum after MA cancellation using (e) acceleration signal and (f) gyroscope signal.

dominant frequency of  $P_S(i)$  overlaps only with that of  $P_A(i)$ . Then, only the acceleration signal provides the correct MA reference of the corrupted PPG signal, which can be observed to minimize or attenuate the dominant frequency power corresponding to the MA corrupting the PPG signal. On the other hand, in the case 2, the dominant frequency of  $P_S(i)$  overlaps only with that of  $P_G(i)$ . Then, only the gyroscope signal provides the correct the MA reference.

The two opposite cases indicate that acceleration and gyroscope signals do not always correctly identify the true MA reference. To complement the acceleration and gyroscope signals, we can consider both signals for MA cancellation by sequentially performing MA cancellation algorithms. However, because the MA cancellation attenuates or eliminates the frequency power of MAs in the PPG signal, sometimes it attenuates or eliminates even the true HR frequency power, particularly when the dominant frequency of an acceleration or gyroscope signal is close to the true HR. In the case 2 shown in Fig. 1(d), the dominant frequency of  $P_A(i)$  overlaps with the dominant frequency of PPG. Then, MA cancellation using both signals may attenuate or eliminate the true HR information. Thus, MA cancellation should be carefully performed to minimize the probability of losing HR information. To avoid such unfortunate circumstance, a better MA cancellation algorithm should be able to select the most suitable MA reference signal between the acceleration and gyroscope signals every time we measure an instantaneous HR. If feasible, we can use a more appropriate MA reference for MA cancellation every time we estimate the HR.

In this study, we proposed the algorithm of adaptive scheduling of acceleration and gyroscope signals to select the most suitable MA reference signal. We first investigated how acceleration and gyroscope signals are correlated with MAs corrupting the PPG signal. For the MA analysis from acceleration and gyroscope signals, we

first derived a mathematical formulation when the swinging arm is unfolded. Then, we extended the formulation to a more realistic condition by partially folding a swinging arm. Given the mathematical investigation, we propose an adaptive MA reference selection approach and evaluate this approach based on state-of-the-art methods [20,22,24,25,29] for MA cancelation and HR estimation.

### 3. MA Reference selection between acceleration and gyroscope signals

#### 3.1. Acceleration and gyroscope characteristics with stretched arm

##### 3.1.1. Model and parameter definition

First, we simplified the model representing the applied forces to the PPG, acceleration, and gyroscope sensors when a stretched arm swings along the trajectory A-B-C-B-A, as shown in Fig. 2. In the model, we defined four forces: an intrinsic force (I), a centrifugal force (C), an arm-swing movement force (M), and a vertical-body movement force (B), all of which change according to the relative position. Consider the wearable device worn on the wrist, moving along the trajectory A-B-C-B-A, where we denote  $\theta$  as the swing angle relative to position B by the positive angle toward position A and the negative angle toward position C. In addition, we denote the angles of centrifugal force and gravity with respect to the x- and y-axes of the accelerator and gyroscope by  $\theta_c^x, \theta_c^y, \theta_I^x$ , and  $\theta_I^y$ , respectively.

##### 3.1.2. Intrinsic Force

We define an intrinsic force as the force applied to the PPG, accelerator, and gyroscope by gravity:  $M_I, A_I$ , and  $G_I$ , respectively. There are no effects of intrinsic forces for the PPG and gyroscope:

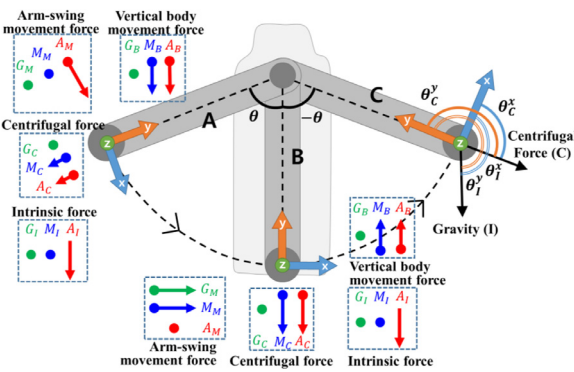


**Fig. 2.** Simplified model with swinging of the stretched arm: this model represents the applied forces to PPG, acceleration, and gyroscope sensors when a stretched arm swings.

$M_I = G_I = 0$ . Moreover, an accelerometer measures the gravitational acceleration in the direction opposite to the forced direction (straight upward) and measures a zero value for free-fall motion. Subsequently,  $A_I$  can be decomposed as follows:

$$A_I = (A_I^x, A_I^y, A_I^z) \approx (g \cdot \cos(\theta_I^x), g \cdot \cos(\theta_I^y), 0) \quad (6)$$

where  $g = -9.81 \text{ m/s}^2$ ,  $\theta_I^x = \theta_C^x - \theta$ , and  $\theta_I^y = \theta_C^y - \theta$ . Under the condition of the stretched arm,  $\theta_C^x = \frac{\pi}{2}$  and  $\theta_C^y = \pi$ . Then:

$$A_I \approx (g \cdot \sin\theta, -g \cdot \cos\theta, 0) \quad (7)$$

Given the trajectory A-B-C-B-A,  $\theta$  changes between  $-\frac{\pi}{2}$  and  $\frac{\pi}{2}$ . More specifically,  $\theta$  continuously changes from  $\theta_{max}$  to 0, 0 to  $-\theta_{max}$ ,  $-\theta_{max}$  to 0, and 0 to  $\theta_{max}$ , where  $\theta_{max}$  is a positive angle smaller than  $\frac{\pi}{2}$  in reality. By wrapping  $\theta$  into  $\theta'$ , which changes from 0 to  $2\pi$ , we obtain:

$$A_I \approx (g \cdot \cos\theta', -g \cdot |\sin\theta'|, 0) \quad (8)$$

Then, during trajectory A-B-C-B-A,  $A_I^x$  exhibits a one-cycle movement, whereas  $A_I^y$  exhibits a two-cycle movement. This indicates that  $A_I$  may result in the two dominant frequencies  $F$  and  $2F$  when a stretched arm swings with a frequency of  $F$ .

### 3.1.3. Centrifugal force

We define centrifugal forces as outward forces to the PPG, accelerometer, and gyroscope when a wrist-worn sensor swings with the trajectory A-B-C-B-A:  $M_C$ ,  $A_C$  and,  $G_C$ , respectively. Regarding a gyroscope, there is no effect of the centrifugal force because the gyroscope measures the angular velocity:  $G_C = 0$ . In addition, the accelerometer and PPG measure the centrifugal force. More specifically, for an accelerometer, the centrifugal force is applied in the y-axis direction (outward from the wrist). Then,  $A_C$  can be decomposed as:

$$A_C = (A_C^x, A_C^y, A_C^z) \approx \left( \frac{(v_C)^2}{l} \cdot \cos(\theta_C^x), \frac{(v_C)^2}{l} \cdot \cos(\theta_C^y), 0 \right), \quad (9)$$

where  $v_C$  is the tangential velocity. As  $\theta_C^x = \frac{\pi}{2}$  and  $\theta_C^y = \pi$ :

$$A_C \approx \left( 0, -\frac{(v_C)^2}{l}, 0 \right). \quad (10)$$

Given the trajectory A-B-C-B-A, the speed  $v_C$  continuously changes from 0 to  $v_{max}$ ,  $v_{max}$  to 0, 0 to  $v_{max}$ , and  $v_{max}$  to 0, where  $v_{max}$  is the maximum speed, which changes the two-cycle movement of  $A_C^y$ . Thus,  $A_C$  results in a dominant frequency of  $2F$  when a stretched arm swings with a frequency of  $F$ . Similarly,  $M_C$  can be decomposed as:

$$M_C = (M_C^x, M_C^y, M_C^z) \approx \left( 0, -\frac{(v_C)^2}{l}, 0 \right). \quad (11)$$

Then,  $M_C$  also results in a dominant frequency of  $2F$  when a stretched arm swings with a frequency of  $F$ .

### 3.1.4. Arm-swing movement force

We define arm-swing movement forces as the forces applied to the PPG, accelerometer, and gyroscope in the tangential direction of the arm swing:  $M_M$ ,  $A_M$ , and  $G_M$ , respectively. With respect to an accelerometer,  $A_M$  can be decomposed as:

$$A_M = (A_M^x, A_M^y, A_M^z) \approx \left( A_M \cdot \cos\left(\theta_C^x - \frac{\pi}{2}\right), A_M \cdot \cos\left(\theta_C^y - \frac{\pi}{2}\right), 0 \right), \quad (12)$$

where  $A_M$  is the acceleration magnitude according to the arm swing. Since  $\theta_C^x = \frac{\pi}{2}$  and  $\theta_C^y = \pi$ , we obtain:

$$A_M \approx (A_M, 0, 0). \quad (13)$$

Given the trajectory A-B-C-B-A,  $A_M$  continuously changes from a positive value to zero, a negative value, zero, and a positive value, which results in a one-cycle movement of  $A_M^x$ . Thus,  $A_M$  results in a dominant frequency of  $F$  when a stretched arm swings with a frequency of  $F$ . Similarly:

$$M_M = (M_M^x, M_M^y, M_M^z) \approx (A_M, 0, 0). \quad (14)$$

Then,  $M_M$  also results in a dominant frequency of  $2F$ . Moreover, regarding a gyroscope, the z-axis rotates and exerts a force only on the z-axis of the gyroscope. Thus,  $G_M$  results in a dominant frequency of  $F$ .

### 3.1.5. Vertical-body movement force

We define a vertical body movement force as the force applied to the PPG, accelerometer, and gyroscope when the entire body moves up and down:  $M_B$ ,  $A_B$ , and  $G_B$ , respectively. Regarding an accelerometer,  $A_B$  can be decomposed as:

$$A_B = (A_B^x, A_B^y, A_B^z) \approx (A_B \cdot \cos(\theta_I^x), A_B \cdot \cos(\theta_I^y), 0), \quad (15)$$

where  $A_B$  is the force magnitude according to the up-down movement. As  $\theta_I^x = \theta_C^x - \theta$ ,  $\theta_I^y = \theta_C^y - \theta$ ,  $\theta_C^x = \frac{\pi}{2}$ , and  $\theta_C^y = \pi$ ,  $A_B$  can be expressed as:

$$A_B \approx (A_B \cdot \sin\theta, -A_B \cdot (\cos\theta), 0). \quad (16)$$

By wrapping  $\theta$  into  $\theta'$ , which changes from 0 to  $2\pi$ , we obtain:

$$A_B \approx (A_B \cdot \cos\theta', -A_B \cdot |\sin\theta'|, 0). \quad (17)$$

Given the trajectory A-B-C-B-A,  $\cos\theta'$  exhibits a one-cycle movement, whereas  $|\sin\theta'|$  exhibits a two-cycle movement. In addition,  $A_B$  exhibits a two-cycle movement because the entire body moves up and down twice during trajectory A-B-C-B-A. Accordingly, given the wrist movement frequency of  $F$ ,  $\cos\theta'$  can be replaced by  $\cos(2\pi F t)$ ,  $|\sin\theta'|$  by  $|\sin(2\pi F t)|$ , and  $A_B$  by  $\sin(2\pi F t)$ . Then:

$$\begin{aligned} A_B^x &= \sin(2\pi 2F t) \cdot \cos(2\pi F t) = \frac{\sin(2\pi(Ft)) + \sin(2\pi(3Ft))}{2} \\ A_B^y &= -\sin(2\pi 2F t) \cdot |\sin(2\pi F t)| \approx -\sin(2\pi 2F t) \cdot (\sin(2\pi F t) + \alpha) \\ &= \frac{1 - \cos(2\pi(4Ft))}{2} - \alpha \sin(2\pi 2F t) \end{aligned} \quad (18)$$

Here,  $A_B^x$  has the two dominant frequencies of  $F$  and  $3F$ , and  $A_B^y$  has the two dominant frequencies of  $2F$  and  $4F$ . Thus,  $A_B$  exhibits the four dominant frequencies of  $F$ ,  $2F$ ,  $3F$ , and  $4F$ . Regarding a PPG sensor,  $M_M$  exhibits the dominant frequency of  $2F$  because the vertical movement (up and down) is repeated twice along the trajectory A-B-C-B-A. Moreover, a gyroscope is not affected by the vertical body movement force because the force is not related to the angular velocity or rotation.

**Table 1** summarizes the possible fundamental frequencies of the PPG, accelerometer, and gyroscope signals when a wearable device worn on the wrist swings along the trajectory A-B-C-B-A with a frequency of  $F$ .

**Table 1**

Fundamental frequencies expressed in MAs in PPG, acceleration, and gyroscope signals when a wearable device worn on the wrist swings with the frequency of  $F$  (Hz) based on Fig. 2.

	Frequencies in PPG	Frequencies in Accelerator			Frequencies in Gyroscope		
		x-axis	y-axis	z-axis	x-axis	y-axis	z-axis
Intrinsic force	0	$F$	$2F$	0	0	0	0
Centrifugal force	$2F$	0	$2F$	0	0	0	0
Arm-swing movement force	$F$	$F$	0	0	0	0	$F$
Vertical body movement force	$2F$	$F, 3F$	$2F, 4F$	0	0	0	0

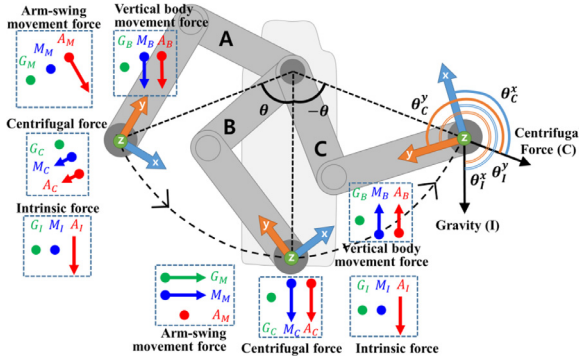


**Fig. 3.** Simplified model with swinging of the partially folded arm: this model represents the applied forces to PPG, acceleration, and gyroscope sensors when a partially folded arm swings.

### 3.2. Acceleration and gyroscope characteristics with partially folded arm

We extended the model to a more realistic case in which the arm is partially folded, as shown in Fig. 3. Similar to the case of the stretched arm, we investigated the four forces applied to the wrist when the sensor on the wrist moves along the trajectory A-B-C-B-A. By partially folding an arm,  $\theta_C^x$  and  $\theta_C^y$  increase:  $\theta_C^x$  is greater than  $\frac{\pi}{2}$ , and  $\theta_C^y$  is greater than  $\pi$ . For simplicity, we assume that  $\theta_C^x = \frac{3\pi}{4}$  and  $\theta_C^y = \frac{5\pi}{4}$ .

#### 3.2.1. Intrinsic force

The intrinsic force  $A_I$  with a partially folded arm can be expressed starting from (6). By partially folding an arm with  $\theta_C^x = \frac{3\pi}{4}$  and  $\theta_C^y = \frac{5\pi}{4}$ ,  $A_I$  in (7) changes to:

$$A_I \approx \left( \frac{\sqrt{2}}{2} g \cdot (-\cos\theta + \sin\theta), -\frac{\sqrt{2}}{2} g \cdot (\cos\theta + \sin\theta), 0 \right) \quad (19)$$

Given the trajectory A-B-C-B-A,  $\theta$  changes between  $-\frac{\pi}{2}$  and  $\frac{\pi}{2}$ : it continuously changes from  $\theta_{max}$  to 0, 0 to  $-\theta_{max}$ ,  $-\theta_{max}$  to 0, and 0 to  $\theta_{max}$ , where  $\theta_{max}$  is a positive angle smaller than  $\frac{\pi}{2}$  in reality. By wrapping  $\theta$  into  $\theta'$ , which changes from 0 to  $2\pi$ , we obtain

$$A_I \approx \left( \frac{\sqrt{2}}{2} g \cdot (-|\sin\theta'| + \cos\theta'), -\frac{\sqrt{2}}{2} g \cdot (|\sin\theta'| + \cos\theta'), 0 \right) \quad (20)$$

Then,  $A_I^x$  and  $A_I^y$  exhibit both one-cycle and two-cycle movements. This indicates that  $A_I$  exhibits two dominant frequencies of  $F$  and  $2F$  when a partially folded arm swings with a frequency of  $F$  (Hz). In addition, for a PPG and gyroscope, there are no intrinsic forces:  $M_I = G_I = 0$ .

#### 3.2.2. Centrifugal force

The centrifugal acceleration  $A_C$  with a partially folded arm can be expressed starting from (9). By partially folding an arm with

$\theta_C^x = \frac{3\pi}{4}$  and  $\theta_C^y = \frac{5\pi}{4}$ ,  $A_C$  in (10) changes to:

$$A_C \approx \left( -\frac{\sqrt{2}}{2} \frac{(v_C)^2}{l}, -\frac{\sqrt{2}}{2} \frac{(v_C)^2}{l}, 0 \right). \quad (21)$$

Given the trajectory A-B-C-B-A, the speed  $v_C$  continuously changes from 0 to  $v_{max}$ ,  $v_{max}$  to 0, 0 to  $v_{max}$ , and  $v_{max}$  to 0, where  $v_{max}$  is the maximum speed, which results in two-cycle movements of  $A_C^x$  and  $A_C^y$ . Thus,  $A_C$  results in a dominant frequency of  $2F$  when a folded arm swings with a frequency of  $F$ . Similarly, the centrifugal force is also applied to the PPG signal, resulting in a dominant frequency of  $2F$ . As the gyroscope measures angular velocity rather than centrifugal force,  $G_C$  does not exist.

#### 3.2.3. Arm-swing movement force

The decomposed arm-swing movement force  $A_M$  with a partially folded arm can start from (12). By partially folding an arm with  $\theta_C^x = \frac{3\pi}{4}$  and  $\theta_C^y = \frac{5\pi}{4}$ ,  $A_M$  in (13) changes to:

$$A_M \approx \left( \frac{\sqrt{2}}{2} A_M, -\frac{\sqrt{2}}{2} A_M, 0 \right), \quad (22)$$

where  $A_M$  is the acceleration magnitude according to the arm swing. Given the trajectory A-B-C-B-A, the force magnitude  $A_M$  continuously changes from  $A_{max}$  to 0, 0 to  $-A_{max}$ ,  $-A_{max}$  to 0, and 0 to  $-A_{max}$ , where  $A_{max}$  is the maximum of  $A_M$ , which results in a one-cycle movement of  $A_M^x$ . Thus, given the wrist movement frequency of  $F$ ,  $A_M$  results in a dominant frequency of  $F$ . Similarly, the arm-swing movement force is also applied to the PPG signal, resulting in a dominant frequency of  $F$ . Regarding the gyroscope,  $G_M$  results in the dominant frequency of  $F$  because the z-axis rotates and exerts a force on the z-axis of the gyroscope.

#### 3.2.4. Vertical-body movement force

The arm-swing movement force  $A_B$  with a partially folded arm can be expressed starting from (15). By partially folding an arm with  $\theta_C^x = \frac{3\pi}{4}$  and  $\theta_C^y = \frac{5\pi}{4}$ ,  $A_B$  in (16) changes to:

$$A_B \approx \left( \frac{\sqrt{2}}{2} A_B (-\cos\theta + \sin\theta), -\frac{\sqrt{2}}{2} A_B (\cos\theta + \sin\theta), 0 \right), \quad (23)$$

where  $A_B$  is the force magnitude according to the up-down movement. By wrapping  $\theta$  into  $\theta'$ , which changes from 0 to  $2\pi$ , we obtain:

$$\begin{aligned} A_B^x &\approx \frac{\sqrt{2}}{2} A_B (-|\sin\theta'| + \cos\theta'), \\ A_B^y &\approx -\frac{\sqrt{2}}{2} A_B (|\sin\theta'| + \cos\theta'). \end{aligned} \quad (24)$$

Given the trajectory A-B-C-B-A,  $\cos\theta'$  exhibits a one-cycle movement, whereas  $|\sin\theta'|$  exhibits a two-cycle movement. Then,  $\cos\theta'$  can be expressed as  $\cos(2\pi F t)$ ,  $|\sin\theta'|$  as  $\sin(2\pi 2F t) + \alpha$ , and  $A_B$  as  $\sin(2\pi 2F t)$ , which can formulate  $A_B^x$  and  $A_B^y$  as:

$$\begin{aligned} A_B^x &\approx \frac{\sqrt{2}}{2} \sin(2\pi 2F t) \cdot \{-|\sin(2\pi 2F t)| + \cos(2\pi F t)\} \\ &\approx \frac{\sqrt{2}}{2} \sin(2\pi 2F t) \cdot \{-(\sin(2\pi 2F t) + \alpha) + \cos(2\pi F t)\} \end{aligned}$$

**Table 2**

Fundamental frequencies expressed in MAs in PPG, acceleration, and gyroscope signals when a wearable device worn on the wrist swings with the frequency of  $F$  (Hz) based on Fig. 3.

	MAs in PPG	Acceleration			Gyroscope		
		x-axis	y-axis	z-axis	x-axis	y-axis	z-axis
Intrinsic force	0	$F, 2F$	$F, 2F$	0	0	0	0
Centrifugal force	$2F$	$2F$	$2F$	0	0	0	0
Arm-swing movement force	$F$	$F$	$F$	0	0	0	$F$
Vertical body movement force	$2F$	$F, 2F, 3F, 4F$	$F, 2F, 3F, 4F$	0	0	0	0

**Table 3**

Selected MA references based on the fundamental frequencies expressed in true MAs, acceleration, and gyroscope signals.

Case	PPG	Acc	Gyro	Selected MA reference
1	$F$	$F$	$F$	Both
2	$F$	$2F$	$F$	Gyro
3	$2F$	$2F$	$F$	Acc
4	Others			None

$$\begin{aligned}
 & \approx \frac{\sqrt{2}}{2} \left\{ -\sin(2\pi 2Ft) (\sin(2\pi 2Ft) + \alpha) \right. \\
 & \quad \left. + \{\sin(2\pi 2Ft) \cdot \cos(2\pi Ft)\} \right\} \\
 & \approx \frac{\sqrt{2}}{2} \left\{ \frac{1 - \cos(2\pi(4Ft))}{2} - \alpha \sin(2\pi(2Ft)) \right\} \\
 & \quad + \left\{ \frac{\sin(2\pi(Ft)) + \sin(2\pi(3Ft))}{2} \right\} \\
 A_B^y & \approx -\frac{\sqrt{2}}{2} \sin(2\pi 2Ft) \cdot \{|\sin(2\pi Ft)| + \cos(2\pi Ft)\} \\
 & \approx -\frac{\sqrt{2}}{2} \sin(2\pi 2Ft) \cdot \{(\sin(2\pi 2Ft) + \alpha) + \cos(2\pi Ft)\} \\
 & \approx -\frac{\sqrt{2}}{2} \left\{ \sin(2\pi 2Ft) (\sin(2\pi 2Ft) + \alpha) \right. \\
 & \quad \left. + \{\sin(2\pi 2Ft) \cdot \cos(2\pi Ft)\} \right\} \\
 & \approx -\frac{\sqrt{2}}{2} \left\{ \frac{\cos(2\pi(4Ft)) - 1}{2} + \alpha \sin(2\pi(2Ft)) \right\} \\
 & \quad + \left\{ \frac{\sin(2\pi(Ft)) + \sin(2\pi(3Ft))}{2} \right\} \tag{25}
 \end{aligned}$$

Thus, given the wrist movement frequency of  $F$ , both  $A_B^x$  and  $A_B^y$  have four dominant frequencies of  $F, 2F, 3F$ , and  $4F$ . Regarding the PPG sensor,  $M_M$  exhibits the dominant frequency of  $2F$  because the vertical movement (up and down) is repeated twice along the trajectory A-B-C-B-A. Moreover, a gyroscope is not affected by the vertical body movement force because the force is not related to the angular velocity or rotation.

Table 2 summarizes the possible fundamental frequencies of the PPG, accelerator, and gyroscope when a wearable device worn on the wrist swings along the trajectory A-B-C-B-A with a frequency of  $F$ .

### 3.3. Adaptive scheduling of acceleration and gyroscope

#### 3.3.1. Adaptive MA reference selection

Based on the fundamental frequencies expressed in PPG, acceleration, and gyroscope signals, we categorized four possible cases, as summarized in Table 3. For case 1, where all fundamental frequencies are the same as  $F$ , either the acceleration or gyroscope signal can be effective for MA cancelation. For case 2, where the fundamental frequencies of PPG and gyroscope signals are  $F$  and that of acceleration is  $2F$ , only a gyroscope signal could be effective for MA cancelation. For case 3, where the fundamental frequencies

**Table 4**

Algorithm for MA selection in the proposed method.

#### Algorithm 1: Adaptive MA Selection

- 
- \*\*  $S_n(i)$ : Normalized PPG signal segment
  - \*\*  $A_n(i)$ : Acceleration signal segment
  - \*\*  $G_n(i)$ : Gyroscope signal segment
  - Apply FFT to  $S_n(i), A_n(i)$ , and  $G_n(i)$
  - Find the frequency corresponding the highest power
    - $F_M$  from  $S_n(i)$
    - $F_A$  from  $A_n(i)$
    - $F_G$  from  $G_n(i)$
  - IF  $F_M = F_A = F_G$ 
    - THEN, either  $A_n(i)$  or  $G_n(i)$  is selected
    - ELSE IF  $F_M = 2F_A = F_G$ 
      - THEN,  $G_n(i)$  is selected
      - ELSE IF  $2F_M = 2F_A = F_G$ 
        - THEN,  $A_n(i)$  is selected
      - ELSE
        - none is selected
    - END IF
    - Perform MA cancelation using the selected reference

---

of the PPG and acceleration signals are  $2F$ , and that of the gyroscope signal is  $F$ , only an acceleration signal can be effective for MA cancelation. For case 4, both gyroscope and acceleration signals are not effective for MA cancelation, which indicates that we do not need to perform MA cancelation in PPG. The case 4 includes the condition where there is no movement on the wrist wearing the sensor while measuring the PPG signal. In addition, the case 4 also includes the condition where the fundamental frequencies of acceleration signals are  $3F$  or  $4F$ , which are not usually related to MAs in PPG.

For each window data, we first should identify one of the four categorized cases, as presented in Table 3. Let us denote the fundamental frequencies from  $P_S(i), P_A(i)$ , and  $P_G(i)$  by  $F_M, F_A$ , and  $F_G$ , respectively. If  $F_M = F_A = F_G$ , then the segment can be considered as case 1: acceleration or gyroscope signals can be employed for MA cancelation. If  $2F_M = 2F_G = F_A$ , the segment can be considered as case 2: the gyroscope signal is available for MA cancelation. If  $F_M = F_A = 2F_G$ , the segment can be considered as case 3: the acceleration signal is available for MA cancelation. Otherwise, acceleration or gyroscope signals cannot be employed as reference for MA cancelation. Table 4 summarizes the adaptive MA selection process.

To evaluate our adaptive MA reference selection, we used five state-of-the-art methods. The first method uses a Wiener filter to attenuate MAs in (4) or (5) [20]. The second method combines

the Wiener filter with a finite state machine (FSM) framework (Wiener-FSM), which evaluates PPG signal quality from the periodogram after MA removal, and provides only HR estimation results with a clean signal [25]. The third method consists of modifying the power spectrum of the PPG signal by emphasizing the power of the frequency corresponding to the previous window HR, which is then applied to the FSM framework (Kernel-FSM) [29]. The fourth and fifth methods employ a single-mode particle filter (SPF) [22] and a multiple mode PF (MPF), respectively [24]. In the previous studies, all of the five methods performed MA cancelation using only an acceleration signal.

### 3.3.2. Evaluation metrics

The accuracy of the algorithm was evaluated by calculating the absolute error (AE) of the estimation.

$$AE(i) = |HR_{\text{Rest}}(i) - HR_{\text{true}}(i)|, \quad (26)$$

where  $HR_{\text{true}}(i)$  is the true HR (bpm) in the  $i$ th segment. The overall evaluation of HR estimation was performed based on the absolute of AE (AAE) (bpm) by dividing the number of windows  $N$ :

$$AAE = \frac{\sum_{i=1}^N AE(i)}{N}, \quad (27)$$

In addition, we plotted the Bland–Altman to compare the estimated HRs and true HRs, and performed linear regression analysis including Pearson correlation coefficients.

## 4. Results and discussions

### 4.1. Data

Our data comprised 12-min three-channel PPG signals acquired on the wrist, three-axis acceleration signals and three-axis gyroscope signals sampled at 50 Hz. We used a reflective PPG sensor (SFH 7070, Osram opto semiconductors, Regensburg, Germany), and the inertial measurement unit (IMU) sensor (LSM6DSMTR, STMicroelectronics, Geneva, Swiss). The dataset was classified into two groups: BAMI-I and BAMI-II. In the BAMI-I dataset ( $n = 24$  subjects), the exercise protocol included 1 min of rest, 2 min of walking at 3–4 km/h for warm-up, 3 min of running at 6–8 km/h, 2 min of walking, 3 min of running at 8–12 km/h, and 1 min of walking to cool down. The subjects were 10 men and 14 women with an average age of  $26.9 \pm 4.8$  years. The entire exercise process was performed on a treadmill. In the BAMI-II dataset ( $n = 23$  subjects), the exercise protocol included 1 min of rest, 2 min of walking for warm-up at 3–4 km/h, 4 min of running at 6–8 km/h, 4 min of walking at 3–4 km/h, and 1 min of rest to cool down. We designed the session to reflect cardiac rehabilitation exercise for cardiac patients with poor exercise ability, in which they normally walk or run by holding a treadmill bar. Thus, during every 4-min session of running and walking, the subjects walked or ran while holding a treadmill bar during the last two minutes of the session. The subjects were 17 men and 6 women with an average age of  $22.0 \pm 1.7$  years. The entire exercise process was performed on a treadmill. Fig. 4 illustrates each exercise protocol in each dataset.

For both datasets, the reference true HRs were measured using ECG data simultaneously recorded by a 24-h Holter monitor (SEER Light, GE Healthcare, Milwaukee, WI, USA). The Holter device was set to record three channels (leads I, V1, and V6) with the commercial Ag/AgCl wet electrodes (2223H, 3M, Saint Paul, MN, USA) placed at the positions for standard ECG measurement. Then, we selected the best-quality channel and confirmed that R peaks were all clearly discernible. Finally, we manually identified the R peaks, and we computed the average RR intervals in each time window for the reference true HRs. All data with the sampling rate of 125 Hz were collected at Wonkwang University by trained personnel

**Table 5**

Based on the fundamental frequencies expressed in true MAs, acceleration, and gyroscope signals, we categorized four possible cases in BAMI-I and II Datasets.

Case	PPG	Acc	Gyro	Percentage	Selected MA reference
1	F	F	F	1.39%	Both
2	F	2F	F	60.28%	Gyro
3	2F	2F	F	32.33%	Acc
4	Others			6.00%	None

from June to July 2018 for BAMI-I and from March to April 2019 for BAMI-II. This study was approved by the Institutional Review Board of Wonkwang University, Republic of Korea (WKUIRB 201805-032-01). All participants provided written informed consent. All raw signals in the BAMI-I and II datasets are publicly downloadable (BAMI-I at <https://github.com/hooseok/BAMI1> and BAMI-II at <https://github.com/hooseok/BAMI2>). Based on the BAMI-I and II datasets, we found that 1.39%, 60.28%, 32.33%, and 6.00% of all the 8-s data segments corresponded to cases 1, 2, 3, and 4, respectively, as summarized in Table 5.

### 4.2. Results

Using the BAMI-I and II datasets ( $n = 47$ ), we compared the four MA reference selection approaches, i.e. with acceleration signal only, with gyroscope signal only, with both signals, and using our proposed adaptive selection. We applied each approach to five different MA cancelation methods: Wiener filter, Wiener filter-FSM, Kernel-FSM, SPF, and MPF. The results in terms of performances are summarized in Table 6, which indicate that our proposed adaptive selection provided a lower AAE for all five MA cancelation methods. We also summarized more detailed AAE values for the 47 individual subjects in Supplementary Table 1.

Furthermore, we also compared the HR estimation performance from our proposed algorithm to those from other existing methods [18,36,37] as summarized in Table 7. The results show that our adaptive MA scheduling provides more accurate HR estimation results than any other methods. This is because our method effectively uses both MA resources from acceleration and gyroscope signals while others use only acceleration signals.

Fig. 5 shows the Bland–Altman and Pearson coefficients plots from both BAMI-I and II datasets according to the four MA reference selection approaches. These results were obtained using the MPF-based HR estimation; results from other four methods are plotted in Supplementary Figs. 1 to 4. For the MPF method, with the adaptive selection approach, the Pearson correlation coefficient was 0.9965 ( $r^2 = 0.9931$ ), and the limit of agreement ranged from -3.96 to 4.03 bpm (mean: 0.04 bpm; SD: 2.04 bpm). Using the acceleration only, the Pearson correlation coefficient was 0.9369 ( $r^2 = 0.8778$ ), and the limit of agreement ranged between -15.95 and 19.24 bpm (mean: 1.65 bpm; SD: 8.98 bpm). With the gyroscope only, the Pearson correlation coefficient was 0.9836 ( $r^2 = 0.9676$ ), and the limit of agreement ranged between -8.32 and 9.03 bpm (mean: 0.35 bpm; SD: 4.42 bpm). Using both signals, the Pearson correlation coefficient was 0.9955 ( $r^2 = 0.9909$ ), and the limit of agreement ranged between -4.52 and 4.61 bpm (mean: 0.05 bpm; SD: 2.33 bpm). Thus, the adaptive selection approach range was narrower than that of the other three selection approaches. The superiority of the adaptive selection approach was also observed using the other four methods (Supplementary Figs. 1 to 4).

Fig. 6 shows the power spectra examples for the three cases (cases 1, 2, and 3) summarized in Table 3. The first column represents  $P_S(i)$ ,  $P_A(i)$ , and  $P_G(i)$ . The second column represents  $P_S(i)$  after MA cancelation using only  $P_A(i)$ . The third column represents

**Table 6**

Performance comparison based on BAM-I and II datasets ( $n = 47$ ) among four MA reference selection approaches: with acceleration signal only, with gyroscope signal only, with both signals, and using our proposed adaptive selection (five different MA cancelation methods of Wiener filter, Wiener filter-FSM, Kernel-FSM, SPF, and MPF were used).

Algorithm	Acceleration				Gyroscope				Both			
	AAE (bpm)				AAE (bpm)				AAE (bpm)			
	Mean	Std.	Min	Max	Mean	Std.	Min	Max	Mean	Std.	Min	Max
Wiener [20]	9.22	5.52	2.06	26.10	6.95	3.34	1.40	15.48	8.88	3.86	3.14	20.41
Adaptive selection with [20]	3.23	2.84	0.92	11.45	2.29	1.94	0.65	10.33	3.19	2.76	0.96	11.45
Wiener-FSM [25]	4.69	5.55	1.14	22.93	3.17	3.38	1.16	16.24	3.43	4.36	0.67	22.49
Adaptive selection with [25]	4.56	6.28	0.98	30.05	2.19	2.26	0.89	15.76	1.73	0.86	0.84	6.47
Kernel-FSM [29]	4.34	4.64	0.69	18.80	1.68	1.61	0.63	11.04	1.37	0.49	0.63	3.05
Adaptive selection with [29]	2.23	2.08	0.76	11.60	1.49	0.62	0.74	4.64	1.27	0.41	0.59	2.02
SPF [22]	3.34	4.64	0.69	18.80	1.68	1.61	0.63	11.04	1.37	0.49	0.63	3.05
Adaptive selection with [22]	2.12	1.47	0.90	8.86	1.49	0.62	0.74	4.64	1.27	0.41	0.59	2.02
MPF [24]	3.34	4.64	0.69	18.80	1.68	1.61	0.63	11.04	1.37	0.49	0.63	3.05
Adaptive selection with [24]	2.12	1.47	0.90	8.86	1.49	0.62	0.74	4.64	1.27	0.41	0.59	2.02

**Table 7**

Comparison among the proposed method and other HR estimation algorithms.

Algorithm	IMAT [36]	Kalman [37]	JOSS [18]	Proposed method (MPF + Adaptive selection)
AAE (bpm)	$18.29 \pm 5.12$	$6.04 \pm 3.99$	$5.33 \pm 5.03$	$1.27 \pm 0.41$

Values are reported as means  $\pm$  standard deviations.

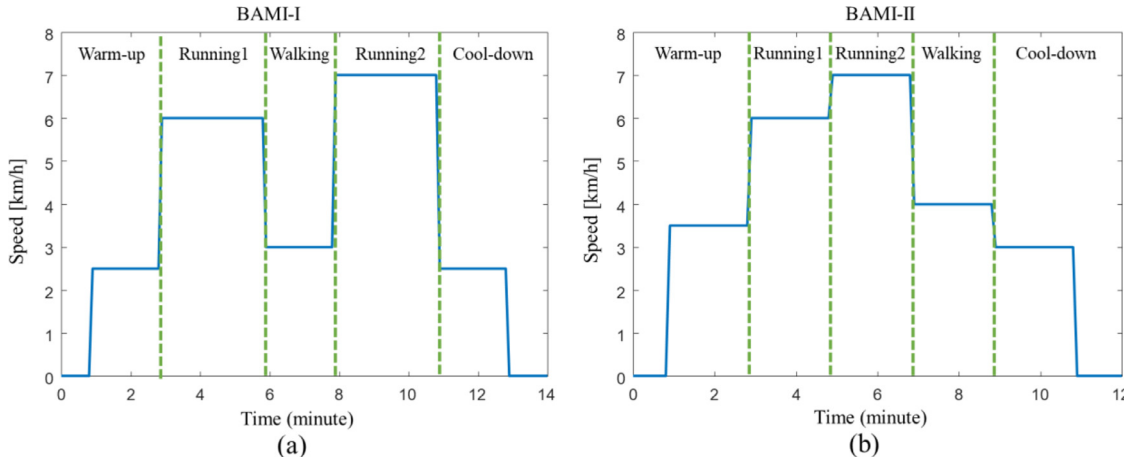


Fig. 4. The exercise protocol in (a) BAM-I and (b) BAM-II.

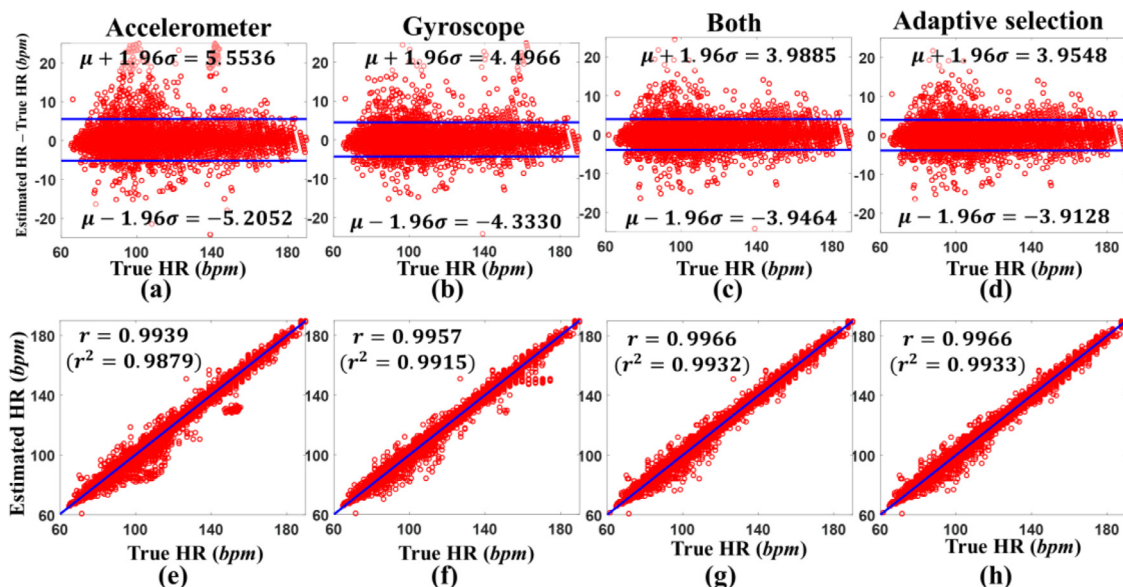
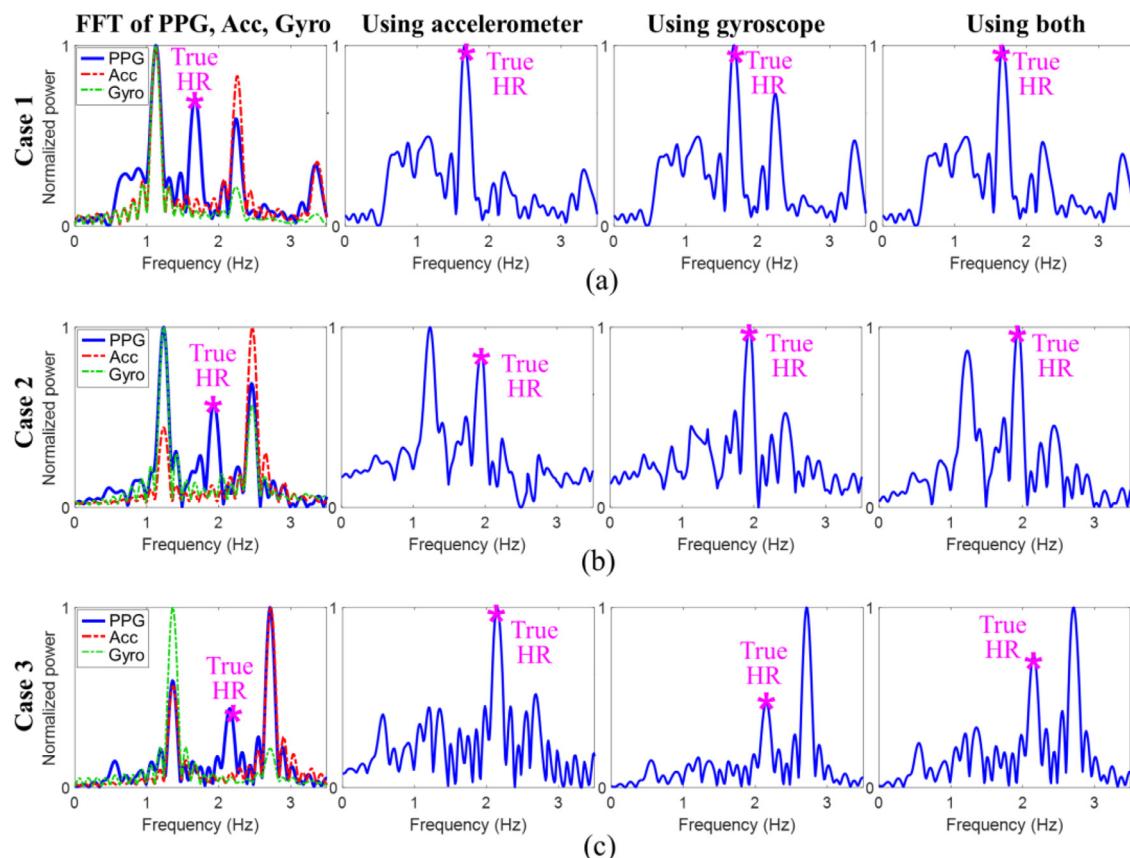


Fig. 5. Bland-Altman plots comparing estimated HRs and true HRs using (a) acceleration-only, (b) gyroscope-only, (c) both, and (d) adaptive selection approach via MPF method. Pearson correlation coefficients and regression line between estimated HRs and true HRs when using (e) acceleration-only, (f) gyroscope-only, (g) both, and (h) adaptive selection approach via MPF method.



**Fig. 6.** Power spectra examples regarding the three cases (cases 1, 2, and 3) summarized in Table 3. The first column depicts the power spectra from PPG, acceleration, and gyroscope signals in each case. The second column shows the power spectrum after MA cancelation using the acceleration signal only. The third and fourth columns depict the power spectra after MA cancelation using the gyroscope signal only and both signals, respectively.

**Table 8**  
Performance comparison according to resting, walking and running from BAM-I and II datasets ( $n = 47$ ).

Condition	Resting	Walking	Running
AAE (bpm)	$1.23 \pm 0.51$	$1.58 \pm 1.17$	$1.73 \pm 3.19$

Values are reported as means  $\pm$  standard deviations.

$P_S(i)$  after MA cancelation using only  $P_G(i)$ . The last column represents  $P_S(i)$  after MA cancelation using both  $P_A(i)$  and  $P_G(i)$ . In case 1, all MA reference selection approaches provided an accurate HR. In case 2, the gyroscope-only and both signal use approaches provided an accurate HR. In case 3, the acceleration-only approach provided an accurate HR. These indicate that our proposed adaptive MA selection leads to perform more accurate MA cancelation.

Table 8 compares the performance according to the different exercise conditions such as resting, walking and jogging.

Fig. 7 shows the HR estimation results from one exemplary subject. Fig. 7(a) shows the fundamental frequencies from  $P_S(i)$ ,  $P_A(i)$ , and  $P_G(i)$  as well as the true HRs for the entire recording time. Fig. 7(b) shows the estimated HRs using only  $P_S(i)$ . Figs. 7(c) to (e) show the estimated HRs after MA cancelation using  $P_A(i)$ ,  $P_G(i)$  and both, respectively. Fig. 7(f) shows the estimated HRs after MA cancelation using our proposed adaptive MA reference selection, where the selection is colored-marked (none, acceleration, gyroscope and both selection). Fig. 7(g) shows the case numbers (case 1, 2, 3 and 4) according to each time segment to appreciate the performance of our algorithm in the challenging exercise cases.

#### 4.3. Real-time deployment in wearable device

Fig. 8 shows our developed wrist-type wearable device using a reflective PPG sensor (SFH 7070, Osram opto semiconductors, Regensburg, Germany) and an IMU sensor (LSM6DSMTR, STMicroelectronics, Geneva, Swiss). The PPG signals obtained from the PPG sensor was converted into a digital signal through an analog front-end (MAX86141, Maxim integrated, San Jose, CA, USA). This analog front-end contains analog-to-digital converters, LED drivers, and an internal switch circuitry. Then, a single IC can control a PPG sensor including an LED and a photodiode. A 1.3-inch liquid crystal display (LCD; KWH013ST03-F01, FORMIKE, Shenzhen, China) and a switch were attached to the front of the device for a user interface device. We applied our proposed algorithm using the digitized signals through a microcontroller (STM32F413CGU6, STMicroelectronics, Geneva, Swiss), and successfully operated HR estimation in real-time with a clock rate of 25 MHz. The average computational time per window was 141 ms, which is operated in real-time.

#### 4.4. Discussions

We observed that when the fundamental frequencies from the MA reference and the true HR overlapped, incorrect results were obtained, as shown in Fig. 9, which is the HR estimation result example from one exemplary subject. Fig. 9(a) shows the HRs computed from fundamental frequencies of PPG and the true HRs for the entire recording time, and Fig. 9(b) shows the estimated HRs using our proposed adaptive MA reference selection approach via Winer-FSM. In the results, we still found erroneous results for the

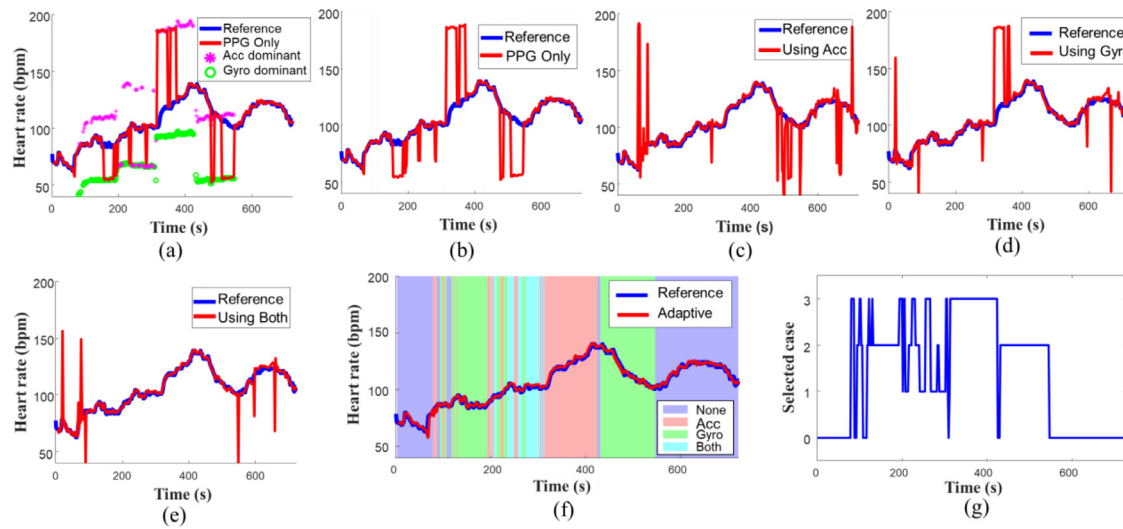


**Fig. 7.** HR estimation results from one exemplary subject: (a) heart rate estimated from PPG, acceleration, and gyroscope signals as well as true HRs for the entire recording time; (b) estimated HRs using PPG signal only; (c) estimated HRs after MA cancelation using acceleration signal only, (d) estimated HRs after MA cancelation using gyroscope signal only; (e) estimated HRs after MA cancelation using both signals, (f) estimated HRs after MA cancelation using our proposed adaptive MA reference selection approach, and (g) adaptively selected cases in real time.

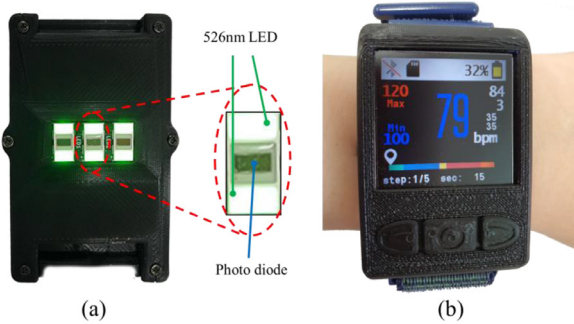


**Fig. 8.** Our developed wrist-type wearable device operated in real-time. Bottom surface with PPG sensor attached (a) and the upper surface with an LCD to check the calculated heart rate (b).

three parts highlighted in orange. We investigated each of the parts and found that the fundamental frequencies from the MA reference and the true HRs overlapped. Fig. 9(c) shows the fundamental frequencies of the PPG, acceleration, and gyroscope signals. The highlighted circles in orange correspond to the erroneous results, where the power spectrum peak from acceleration or gyroscope is overlapped with the true HR. This indicates that even the true HR information was canceled out or attenuated via MA cancellation using the adaptive MA reference. Therefore, previous HR informa-

tion may be needed to preserve the true HR information in PPG signals. For instance, if the fundamental frequency from the MA reference is close to the estimated HR in the previous window, we may not perform MA cancellation or maximally preserve the previous HR information. However, the application of this strategy is challenging because it considers that the previously predicted HR information is correct. For the future work, we also may extend (3) into quadratic transformation of power spectrum and consider cross spectrum between MA-free PPG and MA reference signals. By considering the cross spectrum, the spectrum overlapping issue may be resolved. In addition, if the signal-to-noise ratio is too low, then MA cancellation methods may not work. Thus, for a severely corrupted signal, we should consider other approaches as well as adaptive MA reference selection.

Another issue to be considered is the case 4 in Table 3. We noted that the case 4 mainly includes the condition where there is no movement on the wrist wearing the sensor. However, in the case 4, there are additional possible cases where MA cannot be canceled out. Based on Table 2, when the fundamental frequency of MAs in PPG is 2F, we can expect that that of acceleration is F, 3F or 4F. In these cases, any MA reference cannot cancel out MAs in PPG. Thus, we should investigate the case 4, and find the way how to handle it. The work entails investigating more diverse and realistic models. In the future work, we will extend our proposed algorithm to be applied to MAs with various wrist and arm movements.

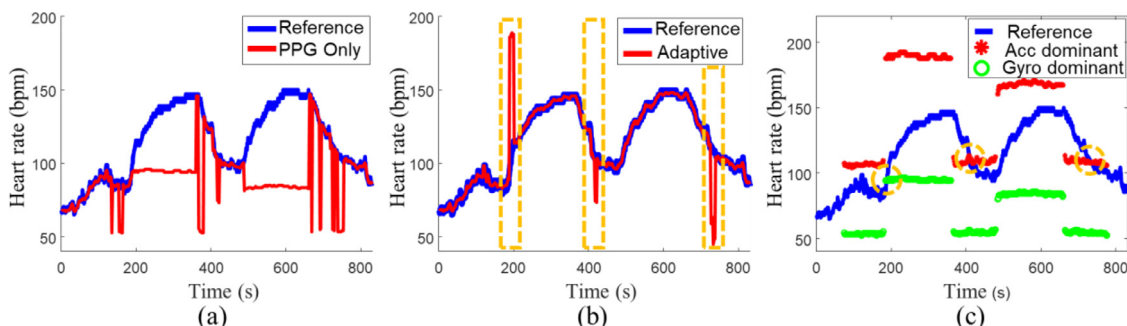


**Fig. 9.** HR estimation result example from one exemplary subject. (a) Estimated HRs computed from fundamental frequencies of PPG and true HRs for the entire recording time, (b) estimated HRs using our proposed adaptive MA reference selection approach, and (c) fundamental frequencies of PPG, acceleration, and gyroscope signals.

Furthermore, our study began with  $P_C(i) \approx P_S(i) - P_A(i)$  or  $P_C(i) \approx P_S(i) - P_G(i)$ . However,  $P_S(i)$  may have additional power spectrum components, which are not related to the movement on the wrist. Typical examples are finger or hand actions such as finger tapping and fist clenching/unfolding, which cause wrist muscle motion corrupting PPG signals not being reflected in the acceleration and gyroscope signals. Thus, in future works, it will be useful to investigate other MA references such as a piezoelectric transducer to identify pressure signals.

## 5. Conclusion

In this study, we first demonstrated that performing HR estimation using PPG signals can be inaccurate when using acceleration only, gyroscope only or both as a MA reference. In order to effectively use the advantages of the MA references from acceleration and gyroscope, we proposed the adaptive MA reference selection approach, which was evaluated through five state-of-the-art methods for MA cancellation and HR estimation. The results showed that our approach improved the HR estimation accuracy for the state-of-the-art methods. Another advantage of our proposed adaptive selection approach is that it is simple to be implemented. It compares the dominant frequencies from PPG, acceleration and gyroscope signals, and selects more appropriate MA reference based on the simple conditions. More importantly, the selection approach can be applied to any method using acceleration and gyroscope signals. We believe that this study will help many researchers studying wearable devices to understand accelerometer and gyroscope sensors. We also expect to open and pave the path to find an appropriate MA reference selection for MA cancellation in PPG. However, our approach could not also resolve the fundamental issue of attenuating true HR information when the fundamental frequencies from the MA reference and the true HR overlapped. In future work, we will investigate the MA cancellation methods considering the case of overlapping MA and HR frequencies. As another limitation, our approach did not consider other types of MAs such as finger tapping and fist clenching/unfolding. Thus, in future work, the development of hardware that minimizes MAs from fingers/hands should be addressed.

## Declaration of Competing Interest

The authors declare that there is no conflict of interest regarding the publication of this paper.

## Acknowledgments

This research was supported by a grant of the Korea Health Technology R&D Project through the Korea Health Industry Development Institute (KHIDI), funded by the Ministry of Health & Welfare, Republic of Korea (grant number: HV22C0233), the Korea Medical Device Development Fund grant funded by the Korea government (the Ministry of Science and ICT; Ministry of Trade, Industry and Energy; Ministry of Health and Welfare; and Ministry of Food and Drug Safety) (KMDF\_PR\_20200901\_0095), and a Basic Science Research Program through National Research Foundation of Korea (NRF) funded by the Ministry of Science, ICT & Future Planning (NRF- 2020R1A2C1014829). This research was also supported by the Italian MIUR PON R&D 2014-2020 AIM project (no. AIM1851228-2. L.F) and supported by the Italian MIUR PRIN 2017 project 2017WZFTZP “Stochastic forecasting in complex systems”.

## Supplementary materials

Supplementary material associated with this article can be found, in the online version, at doi:[10.1016/j.cmpb.2022.107126](https://doi.org/10.1016/j.cmpb.2022.107126).

## References

- [1] M. Radha, P. Fonseca, A. Moreau, M. Ross, A. Cerny, P. Anderer, X. Long, R.M. Aarts, A deep transfer learning approach for wearable sleep stage classification with photoplethysmography, *NPJ Digital Med.* 4 (2021) 1–11.
- [2] D. Castaneda, A. Esparza, M. Ghomari, C. Soltanpur, H. Nazeran, A review on wearable photoplethysmography sensors and their potential future applications in health care, *Int. J. Biosens. Bioelectron.* 4 (2018) 195.
- [3] H. Lee, H. Chung, H. Ko, C. Jeong, S.-E. Noh, C. Kim, J. Lee, Dedicated cardiac rehabilitation wearable sensor and its clinical potential, *PLoS One* 12 (2017) e0187108.
- [4] H. De Cannière, F. Corradi, C.J. Smeets, M. Schouteten, C. Varon, C. Van Hoof, S. Van Huffel, W. Groenendaal, P. Vandervoort, Wearable monitoring and interpretable machine learning can objectively track progression in patients during cardiac rehabilitation, *Sensors* 20 (2020) 3601.
- [5] H. Chung, H. Lee, C. Kim, S. Hong, J. Lee, Patient-provider interaction system for efficient home-based cardiac rehabilitation exercise, *IEEE Access* 7 (2019) 14611–14622.
- [6] S.K. Bashar, D. Han, S. Hajeb-Mohammadalipour, E. Ding, C. Whitcomb, D.D. McManus, K.H. Chon, Atrial fibrillation detection from wrist photoplethysmography signals using smartwatches, *Sci. Rep.* 9 (2019) 1–10.
- [7] T. Pereira, N. Tran, K. Gadhouni, M.M. Pelter, D.H. Do, R.J. Lee, R. Colorado, K. Meisel, X. Hu, Photoplethysmography based atrial fibrillation detection: a review, *NPJ Digital Med.* 3 (2020) 1–12.
- [8] J. Lee, B.A. Reyes, D.D. McManus, O. Maitas, K.H. Chon, Atrial fibrillation detection using an iPhone 4S, *IEEE Trans. Biomed. Eng.* 60 (2012) 203–206.
- [9] K. Lee, H.O. Choi, S.D. Min, J. Lee, B.B. Gupta, Y. Nam, A comparative evaluation of atrial fibrillation detection methods in Koreans based on optical recordings using a smartphone, *IEEE Access* 5 (2017) 11437–11443.
- [10] H.J. Davies, P. Bachtiger, I. Williams, P.L. Molyneaux, N.S. Peters, D.P. Mandic, Wearable in-ear PPG: Detailed respiratory variations enable classification of COPD, *IEEE Trans. Biomed. Eng.* 69 (2022) 2390–2400.
- [11] A. Prabha, J. Yadav, A. Rani, V. Singh, Intelligent estimation of blood glucose level using wristband PPG signal and physiological parameters, *Biomed. Signal Process. Control* 78 (2022) 103876.
- [12] G. Wang, M. Atef, Y. Lian, Towards a continuous non-invasive cuffless blood pressure monitoring system using PPG: Systems and circuits review, *IEEE Circuits Syst. Mag.* 18 (2018) 6–26.
- [13] H.W. Loh, S. Xu, O. Faust, C.P. Ooi, P.D. Barua, S. Chakraborty, R.-S. Tan, F. Molinari, U.R. Acharya, Application of Photoplethysmography signals for Healthcare systems: an in-depth review, *Comput. Methods Programs Biomed.* (2022) 106677.
- [14] S. Heo, S. Kwon, J. Lee, Stress detection with single PPG sensor by orchestrating multiple denoising and peak-detecting methods, *IEEE Access* 9 (2021) 47777–47785.
- [15] M. Zubair, C. Yoon, Multilevel mental stress detection using ultra-short pulse rate variability series, *Biomed. Signal Process. Control* 57 (2020) 101736.
- [16] M.A. Motin, C.K. Karmakar, M. Palaniswami, Ensemble empirical mode decomposition with principal component analysis: A novel approach for extracting respiratory rate and heart rate from photoplethysmographic signal, *IEEE J. Biomed. Health Inform.* 22 (2017) 766–774.
- [17] H. Lee, H. Chung, H. Ko, J. Lee, Wearable multichannel photoplethysmography framework for heart rate monitoring during intensive exercise, *IEEE Sensors J.* 18 (2018) 2983–2993.
- [18] Z. Zhang, Photoplethysmography-based heart rate monitoring in physical activities via joint sparse spectrum reconstruction, *IEEE Trans. Biomed. Eng.* 62 (2015) 1902–1910.
- [19] E. Khan, F. Al Hossain, S.Z. Uddin, S.K. Alam, M.K. Hasan, A robust heart rate monitoring scheme using photoplethysmographic signals corrupted by intense motion artifacts, *IEEE Trans. Biomed. Eng.* 63 (2015) 550–562.
- [20] A. Temko, Accurate heart rate monitoring during physical exercises using PPG, *IEEE Trans. Biomed. Eng.* 64 (2017) 2016–2024.
- [21] Z. Zhang, Z. Pi, B. Liu, TROIKA: A general framework for heart rate monitoring using wrist-type photoplethysmographic signals during intensive physical exercise, *IEEE Trans. Biomed. Eng.* 62 (2014) 522–531.
- [22] Y. Fujita, M. Hiromoto, T. Sato, PARHELIA: Particle filter-based heart rate estimation from photoplethysmographic signals during physical exercise, *IEEE Trans. Biomed. Eng.* 65 (2017) 189–198.
- [23] V. Nathan, R. Jafari, Particle filtering and sensor fusion for robust heart rate monitoring using wearable sensors, *IEEE J. Biomed. Health Inform.* 22 (2017) 1834–1846.
- [24] J. Lee, H. Chung, H. Lee, Multi-mode particle filtering methods for heart rate estimation from wearable photoplethysmography, *IEEE Trans. Biomed. Eng.* 66 (2019) 2789–2799.
- [25] H. Chung, H. Lee, J. Lee, Finite state machine framework for instantaneous heart rate validation using wearable photoplethysmography during intensive exercise, *IEEE J. Biomed. Health Inform.* 23 (2018) 1595–1606.
- [26] A. Reiss, I. Indlekofer, P. Schmidt, K. Van Laerhoven, Deep PPG: large-scale heart rate estimation with convolutional neural networks, *Sensors* 19 (2019) 3079.
- [27] D. Biswas, N. Simões-Capela, C. Van Hoof, N. Van Helleputte, Heart rate estimation from wrist-worn photoplethysmography: a review, *IEEE Sensors J.* 19 (2019) 6560–6570.
- [28] M. Wójcikowski, B. Pankiewicz, Photoplethysmographic time-domain heart rate measurement algorithm for resource-constrained wearable devices and its implementation, *Sensors* 20 (2020) 1783.

- [29] H. Chung, H. Lee, J. Lee, State-dependent Gaussian kernel-based power spectrum modification for accurate instantaneous heart rate estimation, *PLoS One* 14 (2019) e0215014.
- [30] H. Lee, H. Chung, J. Lee, Motion artifact cancellation in wearable photoplethysmography using gyroscope, *IEEE Sensors J.* 19 (2018) 1166–1175.
- [31] A.V. Galvez, A.J. Casson, Nine degree of freedom motion estimation for wrist PPG heart rate measurements, in: 2019 41st Annual International Conference of the IEEE Engineering in Medicine and Biology Society (EMBC), 2019, pp. 3231–3234.
- [32] D. Yang, Y. Cheng, J. Zhu, D. Xue, G. Abt, H. Ye, Y. Peng, A novel adaptive spectrum noise cancellation approach for enhancing heartbeat rate monitoring in a wearable device, *IEEE Access* 6 (2018) 8364–8375.
- [33] K. Xu, X. Jiang, W. Chen, Photoplethysmography motion artifacts removal based on signal-noise interaction modeling utilizing envelope filtering and time-delay neural network, *IEEE Sensors J.* 20 (2019) 3732–3744.
- [34] H. Tanaka, K.D. Monahan, D.R. Seals, Age-predicted maximal heart rate revisited, *J. Am. Coll. Cardiol.* 37 (2001) 153–156.
- [35] R.L. Gellish, B.R. Goslin, R.E. Olson, A. McDONALD, G.D. Russi, V.K. Moudgil, Longitudinal modeling of the relationship between age and maximal heart rate, *Med. Sci. Sports Exerc.* 39 (2007) 822–829.
- [36] M.B. Mashhadí, E. Asadi, M. Eskandari, S. Kiani, F. Marvasti, Heart rate tracking using wrist-type photoplethysmographic (PPG) signals during physical exercise with simultaneous accelerometry, *IEEE Signal Process Lett.* 23 (2015) 227–231.
- [37] A. Galli, C. Narduzzi, G. Giorgi, Measuring heart rate during physical exercise by subspace decomposition and Kalman smoothing, *IEEE Trans. Instrum. Meas.* 67 (2017) 1102–1110.